



Distortion of Magnetic Fields in a Starless Core. V. Near-infrared and Submillimeter Polarization in FeSt 1-457

Ryo Kandori¹, Tetsuya Nagata², Ryo Tazaki³, Motohide Tamura^{1,4,5}, Masao Saito⁴, Kohji Tomisaka⁴,
Tomoaki Matsumoto⁶, Nobuhiko Kusakabe¹, Yasushi Nakajima⁷, Jungmi Kwon⁸,
Takahiro Nagayama⁹, and Ken'ichi Tatematsu⁴

¹ Astrobiology Center of NINS, 2-21-1, Osawa, Mitaka, Tokyo 181-8588, Japan; r.kandori@nao.ac.jp

² Kyoto University, Kitashirakawa-Oiwake-cho, Sakyo-ku, Kyoto 606-8502, Japan

³ Astronomical Institute, Graduate School of Science Tohoku University, 6-3 Aramaki, Aoba-ku, Sendai 980-8578, Japan

⁴ National Astronomical Observatory of Japan, 2-21-1 Osawa, Mitaka, Tokyo 181-8588, Japan

⁵ Department of Astronomy, The University of Tokyo, 7-3-1, Hongo, Bunkyo-ku, Tokyo, 113-0033, Japan

⁶ Faculty of Sustainability Studies, Hosei University, Fujimi, Chiyoda-ku, Tokyo 102-8160, Japan

⁷ Hitotsubashi University, 2-1 Naka, Kunitachi, Tokyo 186-8601, Japan

⁸ Institute of Space and Astronautical Science, Japan Aerospace Exploration Agency, 3-1-1 Yoshinodai, Chuo-ku, Sagami-hara, Kanagawa 252-5210, Japan

⁹ Kagoshima University, 1-21-35 Korimoto, Kagoshima 890-0065, Japan

Received 2018 September 3; revised 2018 October 3; accepted 2018 October 13; published 2018 November 27

Abstract

The relationship between submillimeter dust emission polarization and near-infrared (NIR) H -band polarization produced by dust dichroic extinction was studied for the cold starless dense core FeSt 1–457. The distributions of polarization angles (90° -rotated for the submillimeter) and degrees were found to be very different between submillimeter and NIR wavelengths. The mean polarization angles for FeSt 1-457 at submillimeter and NIR wavelengths are $132^\circ.1 \pm 22^\circ.0$ and $2^\circ.7 \pm 16^\circ.2$, respectively. The correlation between P_H and A_V was found to be linear from the outermost regions to the relatively dense lines of sight of $A_V \approx 25$ mag, indicating that NIR polarization reflects the overall polarization (magnetic field) structure of the core, at least in this density range. The flat P_H/A_V versus A_V correlations were confirmed, and the polarization efficiency was found to be comparable to the observational upper limit. On the other hand, as reported by Alves et al. submillimeter polarization degrees show a clear linearly decreasing trend against A_V from $A_V \approx 20$ mag to the densest center ($A_V \approx 41$ mag), appearing as a “polarization hole” structure. The power-law index for the P_{submm} versus A_V relationship was obtained to be ≈ -1 , indicating that the alignment for the submillimeter-sensitive dust is lost. These very different polarization distributions at submillimeter and NIR wavelengths suggest either that (1) there are different radiation environments at these wavelengths or (2) submillimeter-sensitive dust is localized or (3) a combination of both.

Key words: dust, extinction – ISM: clouds – polarization – stars: formation – stars: magnetic field

1. Introduction

Magnetic fields are thought to play an important role in the formation and evolution of molecular clouds, their cores, stars, and planetary systems (e.g., McKee & Ostriker 2007; Crutcher 2012). Measurements of polarizations produced by dust grains are one of the most powerful tools to probe magnetic field geometry and strength at various wavelengths. According to the general alignment mechanism of interstellar dust grains, the elongated dust grains spin about their axis (minor axis) oriented parallel to the magnetic fields (see Andersson et al. 2015 for a review). Thus, dichroic extinction by dust often observed at optical to near-infrared (NIR) wavelengths can produce incident polarization vectors parallel to the plane-of-sky magnetic fields, and dust emission polarimetry at submillimeter to far-infrared (FIR) wavelengths can obtain polarization vectors perpendicular to the plane-of-sky magnetic fields.

Though magnetic field structure can be traced at various wavelengths, different observing wavelengths are sensitive to the different dust sizes: e.g., optical polarimetry is sensitive to

small size grains and submillimeter polarimetry is sensitive to large size grains. Moreover, the probing depth in column density is different at each wavelength. To understand magnetic field structure as well as dust grain properties, polarimetry at multiple wavelengths is essential.

Dust emission polarimetry, particularly at submillimeter to FIR wavelengths, has proven to be a powerful technique for tracing magnetic field structures in regions of high column density, such as in giant molecular clouds or dark cloud complexes (e.g., Matthews et al. 2002; Houde et al. 2004; Sugitani et al. 2010) and protostellar envelopes (e.g., Girart et al. 2006; Rao et al. 2009). Unlike starlight polarimetry, dust emission polarimetry can probe the (dense) region exactly where dust is emitting. However, it is also known that the “polarization hole” effect, i.e., the phenomenon in which the weakest polarization degree is observed toward the densest central regions, exists in almost every emission polarimetry image (e.g., Matthews et al. 2009; Hull et al. 2014; Brauer et al. 2016). Jones et al. (2015) found that for starless cores in the range of $A_V \gtrsim 20$ mag, the slope of the P_{submm} versus τ becomes ~ -1 , indicating that the grain alignment is lost beyond the depth. Thus, it is not valid that the submillimeter or FIR polarizations reflect the magnetic field structure of overall clouds or cores.



Original content from this work may be used under the terms of the [Creative Commons Attribution 3.0 licence](https://creativecommons.org/licenses/by/3.0/). Any further distribution of this work must maintain attribution to the author(s) and the title of the work, journal citation and DOI.

There are studies that compare submillimeter or FIR emission polarimetry with optical or NIR dichroic extinction polarimetry. Kandori et al. (2007) conducted NIR polarimetry (H band) of the NGC 2024 region. Though the comparison between NIR polarization vectors and those at 100 and 850 μm with 90°-rotation results in a good correlation for the relatively diffuse region ($A_V < 50$ mag), the correlation becomes bad toward the highly obscured molecular ridge region ($A_V \geq 50$ mag). This may be due to the limitation of probing depth at NIR wavelengths, typically $A_V < 50$ mag, or the effect of the polarization hole. Kusakabe et al. (2008) conducted similar studies for the OMC-1 (M42) region, and obtained results indicating that the direction of magnetic fields obtained at NIR (H band) wavelengths is identical to those at 350 μm . Since M42 is not the region deeply embedded in the parent molecular cloud, the effect of limited probing depth at NIR wavelengths does not seem severe. Santos et al. (2017) conducted I band polarimetry toward the Vela-C molecular cloud and compared it with the 500 μm dust emission polarimetry data. The obtained magnetic field directions are generally consistent with each other.

The most detailed comparison study was conducted by Alves et al. (2014, 2015) for the starless dense core FeSt 1-457. FeSt 1-457 is cataloged as a member of the the Pipe Nebula dark cloud complex (as core #109 in Alves et al. 2007; Onishi et al. 1999; Muench et al. 2007), located in the direction of the Galactic center, at a distance of 130^{+24}_{-58} pc (Lombardi et al. 2006). Owing to the core's relatively isolated geometry, simple shape, and plenty of background stars, a density structure study using the Bonnor–Ebert model (Ebert 1955; Bonnor 1956) was conducted based on the measurements of dust extinction at NIR wavelengths (Kandori et al. 2005). The physical properties of the core are well determined, with a radius of $18,500 \pm 1460$ au ($144''$), a mass of $3.55 \pm 0.75 M_\odot$, and a central density of $3.5(\pm 0.99) \times 10^5 \text{ cm}^{-3}$ (Kandori et al. 2005) at a distance of 130 pc (Lombardi et al. 2006).

In the study by Alves et al. (2014, 2015), optical (R band), NIR (H band), and submillimeter (870 μm) polarimetry data were compared with each other. This is the first detailed multiple-wavelength polarization study toward a starless core. Though optical and NIR data show consistent polarization vector angles ($168^\circ \pm 4^\circ$ and $163^\circ \pm 5^\circ$, measured from north to east direction), unlike the previous studies described above, submillimeter data ($130^\circ \pm 12^\circ$) systematically bend from NIR data by $\approx 35^\circ$ in the derived magnetic field direction (Figure 1 of Alves et al. 2014). Moreover, the submillimeter polarization degree clearly decreases from the outer region to the densest center appearing as a polarization hole. Thus, the submillimeter polarization seems not to reflect the overall polarization structure of the core, and the difference in polarization angle between optical/NIR and submillimeter wavelengths may be due to the effect of a polarization hole.

In the analysis by Alves et al. (2014), NIR stellar polarimetry data for the core were the superpositions of polarizations from the core itself and ambient medium. They did not isolate the core polarization. Since the background starlight polarimetry measures the integrated dichroic polarization, the subtraction of the polarization from ambient medium is essential. Kandori et al. (2017a), hereafter Paper I, conducted NIR polarimetry of FeSt 1-457 and a subtraction analysis of the ambient polarization from the core polarization, and found that the magnetic field structure associated with FeSt 1-457 was

hourglass-shaped, which was very different in appearance from the original data (see Section 3.1). The hourglass-shaped polarization distribution was modeled using a simple three-dimensional (3D) polarization model (Kandori et al. 2017b, hereafter Paper II). In Kandori et al. (2018), hereafter Paper III, core polarization was corrected for (1) ambient polarization, (2) depolarization effects of inclined distorted 3D magnetic fields, and (3) magnetic inclination angle toward lines of sight.

In the present study, these NIR polarization data were compared with the submillimeter polarization data (Alves et al. 2014). The derived magnetic field direction, as well as the polarization degree distribution of the submillimeter data, were found to be significantly different from those at NIR wavelengths.

2. Data and Methods

The submillimeter polarimetric data were provided by Alves et al. (2014). Observations were conducted at 345 GHz using the Atacama Path Finder Experiment (APEX) 12 m telescope attached with the LABOCA bolometer and PolKa polarimeter (for the instrument, see Siringo et al. 2004, 2012; Wiesemeyer et al. 2014). The half power beam width (HPBW) at the wavelength is $\sim 20''$. 600 scans, each 2.5 minutes long, were conducted to obtain a total of 25 hr of on-source integration time. The instrumental polarization of their data is about $0.10 \pm 0.04\%$ toward the peak of emission. The data was corrected for instrumental polarizations, and the rms noise of the final submillimeter map was typically ~ 5 mJy/beam. The 87 data points with $P_{\text{submm}}/\delta P_{\text{submm}} \geq 2$ were used.

The NIR polarimetric data of FeSt 1-457 were taken from Paper I. The data were taken using the JHK_s -simultaneous polarimetric imaging instrument SIRPOL (Kandori et al. 2006, polarimetry-mode of the SIRIUS camera: Nagayama et al. 2003) on the IRSF 1.4 m telescope at the South African Astronomical Observatory (SAAO). SIRPOL is a single-beam polarimeter providing a wide field of view ($7'7 \times 7'7$ with a scale of $0''.45 \text{ pixel}^{-1}$). The uncertainty of polarization degree due to sky variation is 0.3% during each exposure. The uncertainty of the measurements of the origin of the polarization angle of the polarimeter (i.e., determination of the correction angle) is less than 3° (see Kandori et al. 2006 and the updates for Kusune et al. 2015).

Figure 1(a) shows the polarization vector map of point sources toward FeSt 1-457. The background image is the intensity image in the H band. The core located at the center of the image and the white circle denote the core radius ($144''$) determined based on the extinction map study (Kandori et al. 2005).

Figure 1(b) shows the polarization vector map of point sources after subtraction of ambient polarization components using the stars located outside the core radius (see, Paper I). The figure is a zoomed-in version of Figure 1(a), showing the region inside the core radius. There are 185 stars available to trace the core magnetic fields. In Figure 1(b), magnetic fields assume a distorted axisymmetric shape reminiscent of an hourglass. The white lines show the best fitting result of magnetic field lines using a parabolic function $y = g + gCx^2$, where g specifies each magnetic field line and C determines the curvature of the magnetic fields. This result serves as the first detection of the hourglass-shaped magnetic fields in dense cores (Paper I).

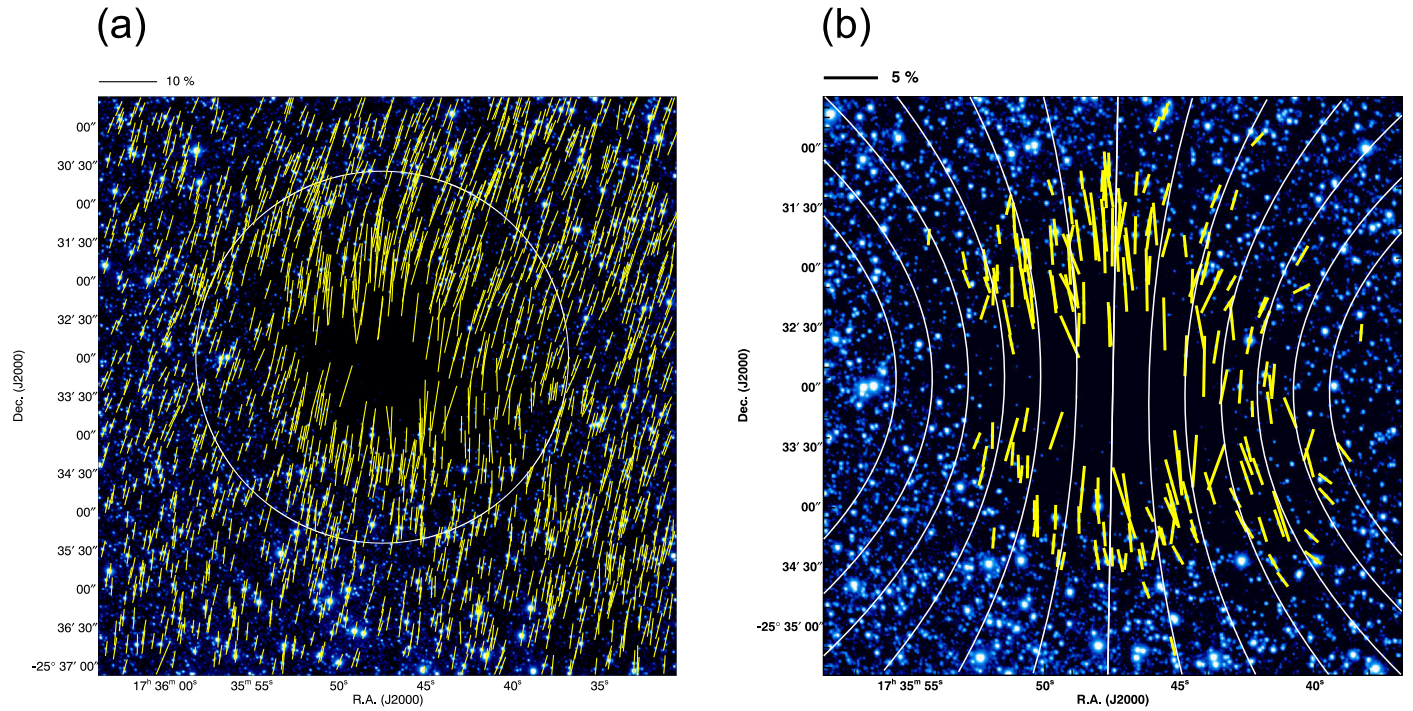


Figure 1. (a) Polarization vectors of point sources in FeSt 1-457 superimposed on the intensity image in the H band. The white circle shows the core radius ($144''$). The scale of the 10% polarization degree is shown above the image. (b) Polarization vectors of FeSt 1-457 after subtracting the ambient polarization component. The field of view is the same as the diameter of the core ($288''$ or 0.19 pc). The white lines indicate the magnetic field direction inferred from the fitting with a parabolic function. The scale of the 5% polarization degree is shown above the image. These figures are taken from Paper I.

The 3D modeling of the hourglass magnetic fields was conducted (Paper II). In the study, the axially symmetric hourglass field was assumed. The 3D function used to model the magnetic fields was a simple parabolic function $z(r, \varphi, g) = g + gCr^2$ in cylindrical coordinates (r, z, φ) , where φ is the azimuth angle (measured in the plane perpendicular to r). The parabolic function describes the orientation of polarization vectors in 3D, and the degree of polarizations can be obtained from the known density structure of the core and the observationally determined polarization-extinction relationship. The polarization vector maps based on the 3D function at various line-of-sight inclination angles are shown in Figure 2 of Paper II. The χ^2 analysis based on the model and the observational data resulted in a line-of-sight inclination angle θ_{inc} of 45° for FeSt 1-457.

When distorted hourglass-shaped fields are inclined toward the line of sight, the model core can produce a depolarization effect, particularly in the equatorial plane of the core (see Figure 2 of Paper II). The depolarization effect is due to the crossing of the polarization vectors located on the front and back sides of the core. In Figure 2 of Paper II, the depolarization effect is apparent, especially in the panels for $\theta_{\text{inc}} = 30^\circ$ and $\theta_{\text{inc}} = 15^\circ$. The depolarization region has dark patches where the polarization degree is low compared with those of neighboring regions.

The polarized light from the core's background stars includes several effects as described above. The superposition of ambient polarization components, the depolarization effect due to inclined distorted magnetic fields, and the magnetic inclination angle should be corrected to obtain accurate polarization information for FeSt 1-457. These effect can be corrected using the subtraction analysis and 3D polarization modeling of the core (Paper III).

3. Results and Discussion

3.1. Comparison between NIR and Submillimeter Polarization

Though comparisons of submillimeter and NIR polarizations have been reported by Alves et al. (2014, 2015), their NIR data were uncorrected with the superposition of ambient polarization, depolarization effects of 3D distorted fields, and line-of-sight magnetic inclination angles. In this section, we compare the NIR data with appropriate corrections with submillimeter polarization data, and discuss the consistency between these data.

Figure 2(a) shows the hourglass-shaped polarization distribution (Paper I) on the A_V distribution measured with $34''$ resolution (Kandori et al. 2005). The peak A_V is ≈ 41 mag toward the center of the core. The central region with A_V greater than ≈ 25 mag of the core is too dense to be probed with the current sensitivity of NIR polarization measurements. The plane-of-sky magnetic axis of the hourglass field is 179° , and the polarization distribution is clearly in the north-south direction, which is perpendicular to the elongation of the densest region of the core, consistent with (1) the mass accumulation along the magnetic field lines (e.g., Galli & Shu 1993a, 1993b) or (2) the magnetohydrostatic configuration (Tomisaka et al. 1988).

Figure 2(b) shows the submillimeter polarization distribution taken from Alves et al. (2014), which was 90° -rotated to show the direction of the magnetic fields. The magnetic field directions obtained from the NIR and submillimeter data differ significantly. The submillimeter vectors flow from northwest to southeast, which does not match the north-south magnetic field distribution obtained at NIR wavelengths. Though the regions traced by both wavelengths are different, the orientations of submillimeter and NIR vectors clearly differ in their

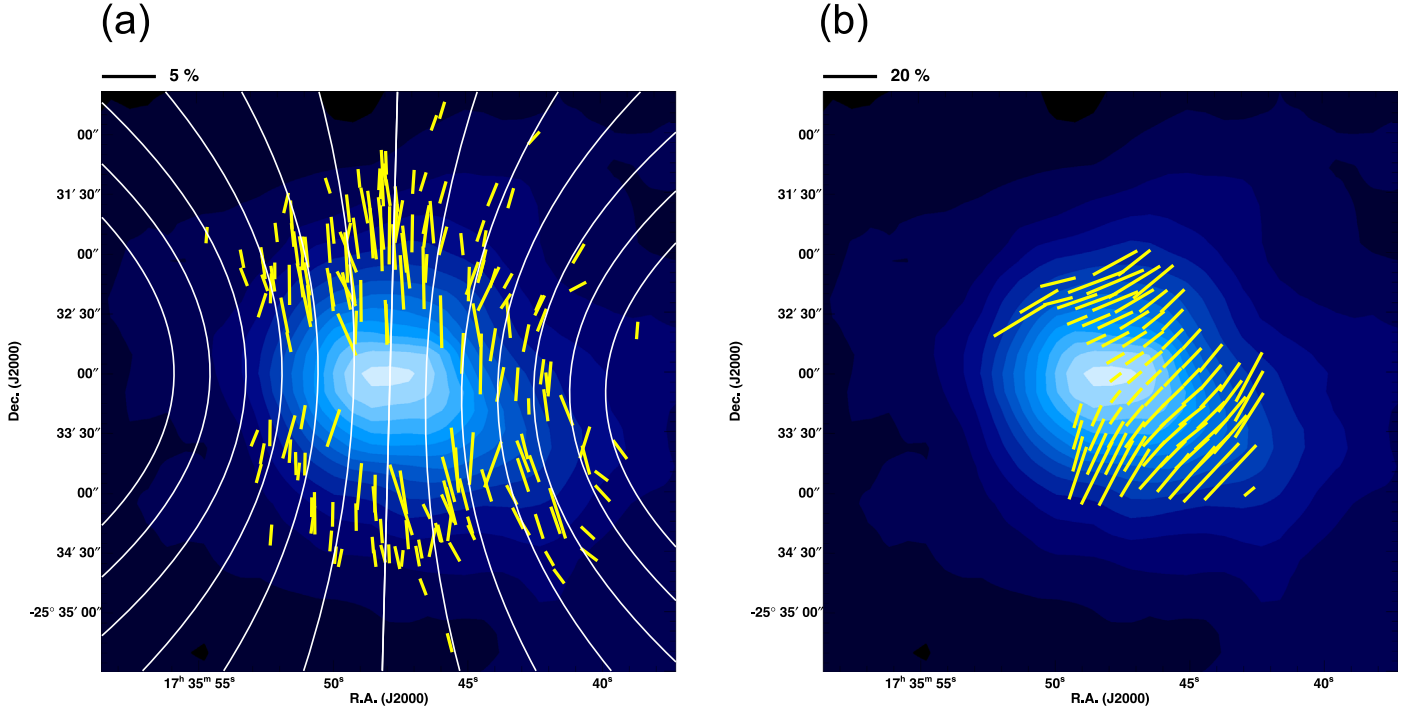


Figure 2. (a) Polarization vectors of FeSt 1-457 in the H band after subtracting the ambient polarization component, superimposed on the A_V map ($33''$ resolution) taken from Kandori et al. (2005). The filled contour starts from 0 mag with a step of 3 mag. The field of view is the same as the diameter of the core ($288''$ or 0.19 pc). The white lines indicate the magnetic field direction inferred from fitting with a parabolic function. The scale of the 5% polarization degree is shown above the image. (b) Polarization vectors of FeSt 1-457 at submillimeter wavelengths (345 GHz) taken from Alves et al. (2014). The polarization vectors were 90° -rotated to show the direction of the magnetic fields. The background image is the same as Figure 2(a). The scale of the 20% polarization degree is shown above the image.

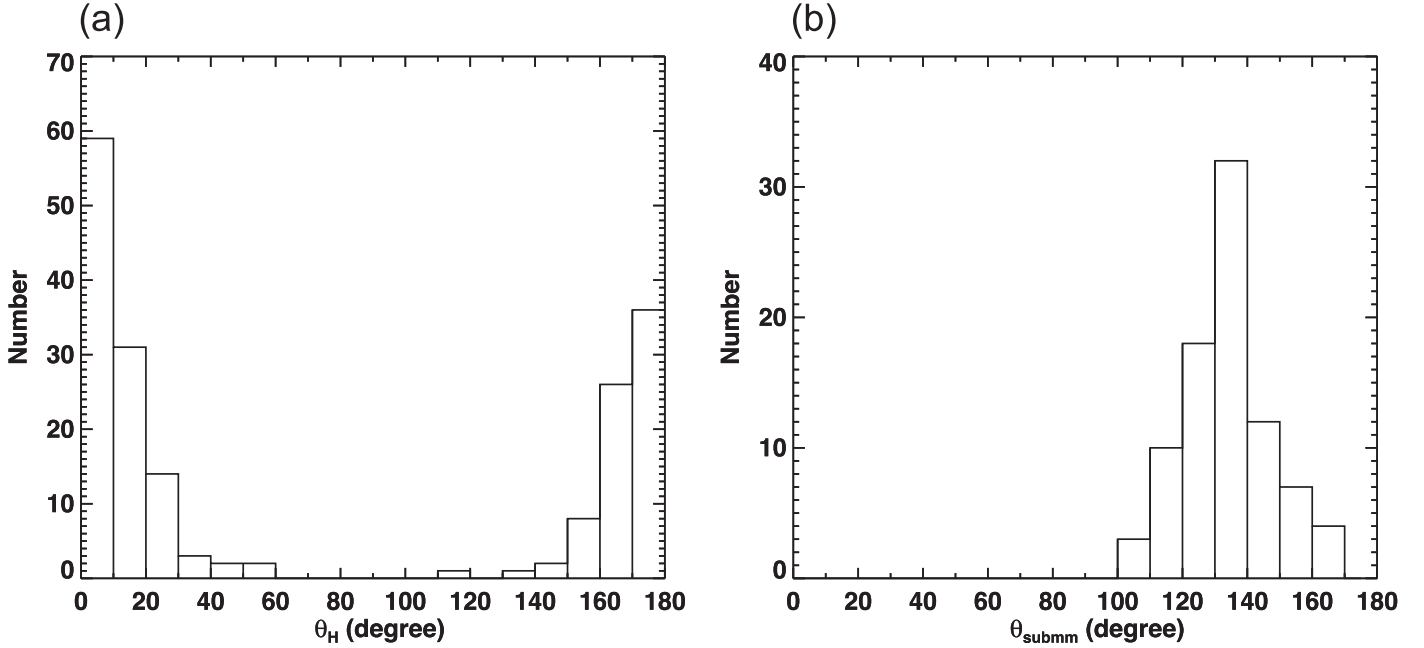


Figure 3. (a) Histogram of θ_H for FeSt 1-457 after subtraction of the ambient polarization component. (b) Histogram of θ_{submm} (90° -rotated) for FeSt 1-457

overlapping regions. Figures 3(a) and (b) show histograms of the NIR polarization vectors and the submillimeter vectors as well (90° -rotated). The mean angles and standard deviations of the distribution at NIR and submillimeter wavelengths are 2.7 ± 16.2 and 132.1 ± 22.0 , respectively. There is a deviation angle of $\approx 50^\circ$ between these data. The submillimeter data also deviate by $\approx 30^\circ$ from the directions of “off-core”

vectors obtained at NIR (165° , Paper I) and at optical ($165^\circ \pm 4^\circ$, Franco et al. 2010) wavelengths.

Figure 4(a) shows the polarization versus A_V relationship at NIR wavelengths, under the corrections of (1) ambient polarization, (2) depolarization caused by 3D distorted fields, and (3) line-of-sight magnetic inclination angle (see, Paper III). The horizontal axis was not from the A_V mapping data in

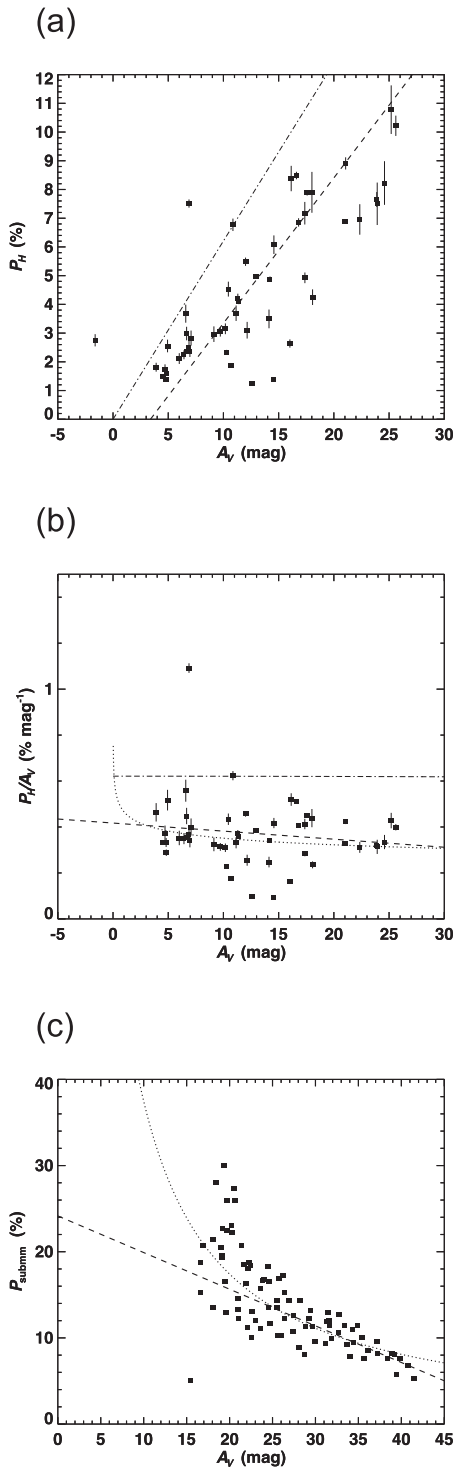


Figure 4. (a) Relationship between polarization degree at H and A_V toward background stars of FeSt 1-457. Stars with $R \leq 144''$ and $P_H/\delta P_H \geq 10$ are plotted. The relationship was corrected for ambient polarization components, the depolarization effect, and the magnetic inclination angle. The dashed line denotes the linear least-squares fit to all the data points. The dotted-dashed line shows the observational upper limit reported by Jones (1989). (b) The relationship of Figure 4(a) divided by A_V (polarization efficiency). The dashed line denotes the linear least-squares fit to the data points. The dotted line shows the power-law fitting result. The dotted-dashed line shows the observational upper limit reported by Jones (1989). (c) Relationship between polarization degree at submillimeter wavelengths and A_V . The dashed line denotes the linear least-squares fit to the data points with $A_V \geq 23$ mag. The dotted line shows the power-law fitting result.

Kandori et al. (2005), but from the $H - K_s$ colors of stars. A_V was calculated using the relation $A_V = 21.7 \times E_{H-K_s}$ (Nishiyama et al. 2008), and $E_{H-K_s} = (H - K_s) - \langle H - K_s \rangle_{\text{bkg}}$, where $\langle H - K_s \rangle_{\text{bkg}} = 0.40$ mag is the average $H - K_s$ color of stars in the same reference field region used in the previous dust extinction study (see Figure 2 of Kandori et al. 2005).

From Figure 4(a), it is clear that the relationship is linear, and the linear least-squares fitting result is $P_H = (0.51 \pm 0.03)A_V - (1.72 \pm 0.46)$. The dotted-dashed line shows the observational upper limit of the relationship described using the equation $P_{K,\text{max}} = \tanh \tau_p$, where $\tau_p = (1 - \eta)\tau_K/(1 + \eta)$ when the parameter η is set to 0.875 (Jones 1989). τ_K denotes the optical depth in the K band. The observed slope in the polarization-extinction relationship for FeSt 1-457 seems comparable to that for the upper limit value. The linear relationship is reflected in the flat distribution of P_H/A_V versus the A_V diagram (Figure 4(b)), linearly fitted as $P_H/A_V = -0.0035A_V + 0.4172$ (dashed line). The fitting of P_H/A_V versus A_V data using the power law $P_H/A_V \propto A_V^\alpha$ (dotted line) resulted in the α index being close to zero, -0.12 ± 0.11 . The power-law fitting result seems identical to the linear fitting line. The dotted-dashed line in the figure shows an observational upper limit in the P/A - A relationship (Jones 1989).

As shown in Figures 4(a) and (b), the relationship between P_H and A_V is linear for the A_V below ≈ 25 mag, with high polarization efficiency comparable to that for the observational upper limit (Jones 1989). This indicates that the NIR polarimetry traces the overall polarization (magnetic field) structure of FeSt 1-457, although the probing depth ($A_V \leq 25$ mag) is not sufficient for the densest regions ($A_V \approx 41$ mag). The simplest interpretation is that, at least $A_V \leq 25$ mag, the polarization efficiency per dust grains at NIR wavelengths is constant from the outer boundary toward the central regions. Alves et al. (2014) reported that there is a kink at $A_V \approx 9.5$ mag in the P_H/A_V versus A_V relationship. Note that they did not conduct any correction to separate core polarizations from ambient polarizations. The kink disappeared after the corrections of (1) described above (Figure 4 of Paper III), which isolate the core polarizations from the effects of ambient medium.





Figure 4(c) shows the submillimeter polarization degree P_{submm} versus A_V diagram. The A_V data were taken from Kandori et al. (2005). Unlike NIR, submillimeter polarization degree data clearly show a decreasing trend against A_V , fitted as $P_{\text{submm}} = (-0.43 \pm 0.08)A_V + (24.2 \pm 2.6)$. In the fitting, the data below $A_V = 23$ mag were ignored. The steep rise of P_{submm} at $A_V < 23$ mag may be real, and may indicate the steep increase of polarization efficiency at submillimeter wavelengths toward the outer regions. The fitting of P_{submm} versus A_V using the power law $P_{\text{submm}} \propto A_V^\alpha$ (dotted line) resulted in an α index of -1.11 ± 0.12 . The obtained index close to -1 indicates that the alignment of submillimeter-sensitive dust is lost inside the core. This is consistent with the value, -0.92 ± 0.17 , obtained by Alves et al. (2014), and is also consistent with the observational report for other starless cores (Jones et al. 2015). The distribution of P_{submm} slightly deviates from the power-law fitting (dotted line) toward the low A_V region. This may be indicative of the alignment of dust grains in the outer region of the core.

Figures 4(a)–(c) are dramatically different. The polarization degree relationships against A_V at NIR and submillimeter

wavelengths are found to be very different in FeSt 1–457. Though the existence of a polarization hole at submillimeter wavelengths may be a sign of the lack of radiation in the starless core according to the radiative torque theory (e.g., Dolginov & Mitrofanov 1976; Draine & Weingartner 1996, 1997; Lazarian & Hoang 2007), the linear P_H versus A_V relationship requires relatively strong radiation fields. A possible explanation for this is the difference in the radiation environments of FeSt 1–457 at NIR and submillimeter wavelengths. Another possible explanation is the localization of submillimeter-sensitive dust in the core. As discussed by Alves et al. (2014), large dust in a deep core interior does not contribute to the submillimeter polarization and dust in the outer region may be relatively well traced by submillimeter polarimetry. This scenario may explain large difference in magnetic field directions obtained at NIR and submillimeter wavelengths. If this is true, the polarization measurements at submillimeter wavelengths may not be appropriate for probing the densest region of starless dense cores. With linear correlations against A_V , NIR polarization is proven to be a robust and accurate tool for studying magnetic fields toward the outer region to the relatively obscured ($A_V \approx 25$ mag) lines of sight. To investigate magnetic field and polarization efficiency in the innermost regions, deep NIR polarimetries with unprecedented depths using large 8 m class telescopes are planned.

We are grateful to the staff of SAAO for their kind help during the observations. We wish to thank Tetsuo Nishino, Chie Nagashima, and Noboru Ebizuka for their support in the development of SIRPOL, its calibration, and its stable operation with the IRSF telescope. The IRSF/SIRPOL project was initiated and supported by Nagoya University, the National Astronomical Observatory of Japan, and the University of Tokyo in collaboration with the South African Astronomical Observatory under the financial support of Grants-in-Aid for Scientific Research on Priority Area (A) No. 10147207 and 10147214, and Grants-in-Aid No. 13573001 and 16340061 of the Ministry of Education, Culture, Sports, Science, and Technology of Japan. R.K., M.T., N.K., K.T. (Kohji Tomisaka), and M.S. also acknowledge support by additional Grants-in-Aid Nos. 16077101, 16077204, 16340061, 21740147, 26800111, 16K13791, 15K05032, and 16K05303.

ORCID iDs

Ryo Kandori  <https://orcid.org/0000-0003-2610-6367>
 Motohide Tamura  <https://orcid.org/0000-0002-6510-0681>
 Masao Saito  <https://orcid.org/0000-0003-0769-8627>
 Kohji Tomisaka  <https://orcid.org/0000-0003-2726-0892>

Tomoaki Matsumoto  <https://orcid.org/0000-0002-8125-4509>

Jungmi Kwon  <https://orcid.org/0000-0003-2815-7774>

Ken'ichi Tatematsu  <https://orcid.org/0000-0002-8149-8546>

References

- Alves, F. O., Frau, P., Girart, J. M., et al. 2014, *A&A*, **569**, 1
 Alves, F. O., Frau, P., Girart, J. M., et al. 2015, *A&A*, **574**, C4
 Alves, J., Lombardi, M., & Lada, C. 2007, *A&A*, **462**, 17
 Andersson, B.-G., Lazarian, A., & Vaillancourt, J. E. 2015, *ARA&A*, **53**, 501
 Bonnor, W. B. 1956, *MNRAS*, **116**, 351
 Brauer, R., Wolf, S., & Reissl, S. 2016, *A&A*, **588**, 129
 Crutcher, R. M. 2012, *ARA&A*, **50**, 29
 Dolginov, A. Z., & Mitrofanov, I. G. 1976, *Ap&SS*, **43**, 291
 Draine, B. T., & Weingartner, J. C. 1996, *ApJ*, **470**, 551
 Draine, B. T., & Weingartner, J. C. 1997, *ApJ*, **480**, 633
 Ebert, R. 1955, *ZA*, **37**, 217
 Franco, G. A. P., Alves, F. O., & Girart, J. M. 2010, *ApJ*, **723**, 146
 Galli, D., & Shu, F. 1993a, *ApJ*, **417**, 220, (paper a)
 Galli, D., & Shu, F. 1993b, *ApJ*, **417**, 243, (paper b)
 Girart, J. M., Rao, R., & Marrone, D. P. 2006, *Sci*, **313**, 812
 Houde, M., Dowell, C. D., Hildebrand, R. H., et al. 2004, *ApJ*, **604**, 717
 Hull, C. L. H., Plambeck, R. L., Kwon, W., et al. 2014, *ApJS*, **213**, 13
 Jones, T. J. 1989, *ApJ*, **346**, 728
 Jones, T. J., Bagley, M., Krejny, M., Andersson, B.-G., & Bastien, P. 2015, *AJ*, **149**, 31
 Kandori, R., Kusakabe, N., Tamura, M., et al. 2006, *Proc. SPIE*, **6269**, 159
 Kandori, R., Nakajima, Y., Tamura, M., et al. 2005, *AJ*, **130**, 2166
 Kandori, R., Tamura, M., Kusakabe, N., et al. 2007, *PASJ*, **59**, 487
 Kandori, R., Tamura, M., Kusakabe, N., et al. 2017a, *ApJ*, **845**, 32, (Paper I)
 Kandori, R., Tamura, M., Nagata, T., et al. 2018, *ApJ*, **857**, 100, (Paper III)
 Kandori, R., Tamura, M., Tomisaka, K., et al. 2017b, *ApJ*, **848**, 110, (Paper II)
 Kusakabe, N., Tamura, M., Kandori, R., et al. 2008, *PASJ*, **136**, 621
 Kusune, T., Sugitani, K., Miao, J., et al. 2015, *ApJ*, **798**, 60
 Lazarian, A., & Hoang, T. 2007, *MNRAS*, **378**, 910
 Lombardi, M., Alves, J., & Lada, C. 2006, *A&A*, **454**, 781
 Matthews, B. C., Fiege, J. D., & Moriarty-Schieven, G. 2002, *ApJ*, **569**, 304
 Matthews, B. C., McPhee, C. A., Fissel, L. M., & Curran, R. L. 2009, *ApJS*, **182**, 143
 McKee, C. F., & Ostriker, E. C. 2007, *ARA&A*, **45**, 565
 Muench, A. A., Lada, C. J., Rathborne, J. M., Alves, J. F., & Lombardi, M. 2007, *ApJ*, **671**, 1820
 Nagayama, T., Nagashima, C., Nakajima, Y., et al. 2003, *Proc. SPIE*, **4841**, 459
 Nishiyama, S., Nagata, T., Tamura, M., et al. 2008, *ApJ*, **680**, 1174
 Onishi, T., Kawamura, A., Abe, R., et al. 1999, *PASJ*, **51**, 871
 Rao, R., Girart, J. M., Marrone, D. P., Lai, S., & Schnee, S. 2009, *ApJ*, **707**, 921
 Santos, F. P., Ade, P. A. R., Angil , F. E., et al. 2017, *ApJ*, **837**, 161
 Siringo, G., Kov cs, A., Kreysa, E., et al. 2012, *Proc. SPIE*, **8452**, 06
 Siringo, G., Kreysa, E., Reichertz, L. A., & Menten, K. M. 2004, *A&A*, **422**, 751
 Sugitani, K., Nakamura, F., Tamura, M., et al. 2010, *ApJ*, **716**, 299
 Tomisaka, K., Ikeuchi, S., & Nakamura, T. 1988, *ApJ*, **335**, 239
 Wiesemeyer, H., Hezareh, T., Kreysa, E., et al. 2014, *PASP*, **126**, 1027